Sub-3 nm Co_3O_4 Nanofilms with Enhanced Supercapacitor Properties

Chao Feng,[†] Jinfeng Zhang,[†] Yu He,[‡] Cheng Zhong,[*,§] Wenbin Hu,[†,‡,§] Lei Liu,[†] and Yida Deng[*,‡]

[†]State Key Laboratory of Metal Matrix Composites, Shanghai Jiao Tong University, Shanghai 200240, People's Republic of China and [‡]Tianjin Key Laboratory of Composite and Functional Materials and [§]Key Laboratory of Advanced Ceramics and Machining Technology (Ministry of Education), Tianjin University, Tianjin 300072, People's Republic of China

ABSTRACT Two-dimensional materials often show a range of intriguing electronic, catalytic, and optical properties that differ greatly from conventional nanoparticles. Herein, we demonstrate the large-scale preparation of sub-3 nm atomic layers Co_3O_4 nanofilms with a nonsurfactant and substrate-free hydrothermal method. This successful preparation of ultrathin nanofilms highlighted the reconstruction of cobalt–ammonia complexes and synergistic effect of free ammonia and nitrate on film growth control. Subsequent performance tests uncovered that these sub-3 nm atomic layer Co_3O_4 nanofilms exhibited an ultrahigh specific capacitance of 1400 F/g in the first galvanostatic charge/discharge test. The specific capacitance of Co_3O_4 nanofilms only slightly decayed less than 3% after 1500 cycling tests. With some parameter adjustments, similar $Co(OH)_2$ nanofilms with a thickness of 3.70 ± 0.10 nm were also prepared. The $Co(OH)_2$ nanofilms possessed maximum specific capacitance of 1076 F/g and peak performance attenuation of about 2% after a cycle stability test.

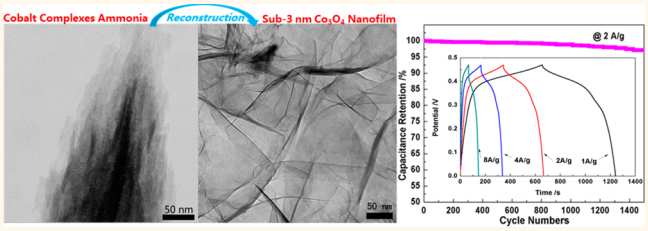

KEYWORDS: atomic layers · Co_3O_4 nanofilms · cobalt–ammonia complexes · hydrothermal · supercapacitor

Nanomaterial research is a rapidly growing branch of materials research due to its considerable potential applications in new energies, catalysts, biomaterials, and applied chemistry.[1,2] Recently, studies on flexible components have increased, and countless efforts have been devoted to the exploitation of these functional nanomaterials.[3−9] In order to improve electrochemical or catalytic performances in device applications by increasing the specific surface area and facilitating the charge transfer during an electrochemical process, two-dimensional (2D) nanostructures seem to be the most practical option.[8,9] The thin nanofilms could not only greatly increase the specific surface area but also facilitate the charge transfer during the electrochemical process. Until now, there have been numerous attempts focused on the fabrications and applications of nanofilms. Zhang prepared zinc oxide nanofilms on a zinc substrate that is used for high-performance electrochemical sensors.[10] Kao also synthesized hierarchically structured supramolecular nanofilms which surely have great potential as functional nanomaterials.[11] Sumboja developed an asymmetric supercapacitor composed of reduced graphene oxide with manganese dioxide paper, in which the similar membrane morphologies of constituents could amplify the synergistic effect.[12]

Since the energy demand is ever-growing, transition-metal-based oxides or hydroxides, such as IrO_2,[13] MnO_2,[14] NiO,[15] V_2O_5,[16] $Co(OH)_2$,[17−19] and $Ni(OH)_2$,[20,21] serve as promising electrode materials in energy storage. Among these available pseudocapacitive materials, cobalt hydroxides or oxides are favorable candidates for application in electrochemical capacitors due to their low cost, great reversibility, and high specific capacitance.[22] Varieties of Co_3O_4 nanostructures were synthesized, and their properties, such as nanocubes,[23] nanosheets,[24] or nanospheres,[25] were investigated. However, there are only a few literature reports about the facile synthesis of 2D Co_3O_4 nanofilms.[26−29] Significant challenges still remain for fabricating these perfect nanofilms with a large area in a comparatively economic and efficient way. More importantly, after the template or

* Address correspondence to yida.deng@tju.edu.cn, cheng.zhong@tju.edu.cn.

Received for review November 18, 2014 and accepted January 22, 2015.

Published online January 22, 2015
10.1021/nn506548d

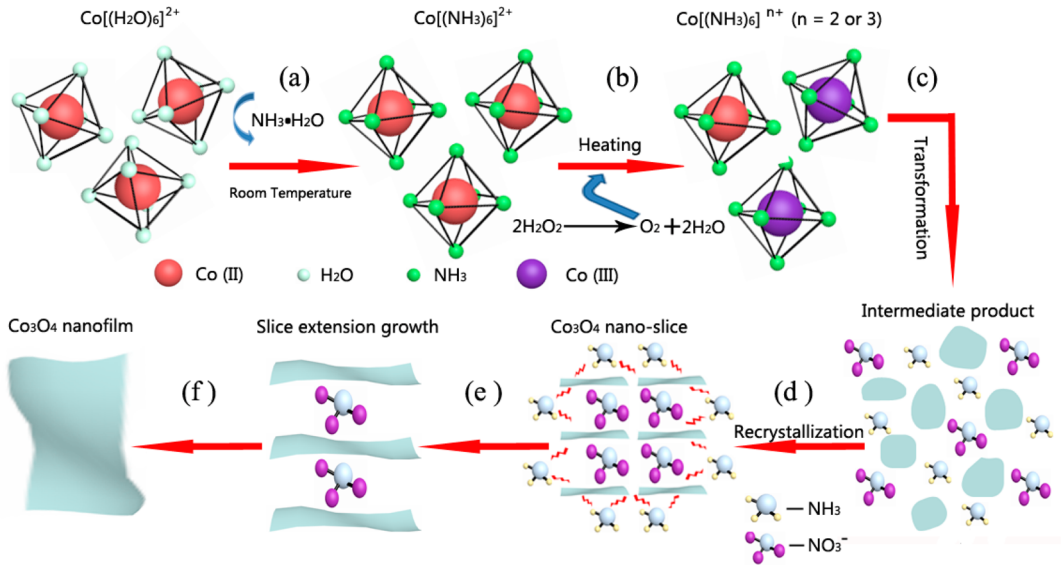

Figure 1. Schematic of the formation of atomic layer Co_3O_4 nanofilms.

deposition technique was applied, usually, a subsequent calcination process was indispensable for preparing perfect Co_3O_4 nanofilms, which added much uncertainty about morphology control and reproducibility.

In this report, we proposed a facile one-step hydrothermal route to prepare sub-3 nm atomic layer Co_3O_4 nanofilms on a large scale for the first time. Without the presence of substrate and organic additive, ultrathin atomic layers of freestanding Co_3O_4 nanofilms with a thickness of 2.90 $\pm$ 0.10 nm were obtained. This method highlighted the reconstruction of cobalt–ammonia complexes under a high concentration of ammonia during hydrothermal conditions, for which the crystallization of 2D structures and the growth of Co_3O_4 greatly relied on the synergistic effect of NH_3 and NO_3^-. The sub-3 nm Co_3O_4 nanofilms exhibited very high specific capacitance of 1400 F/g in the first charge and discharge evaluation and showed stable capacity after 1500 cycling tests. The ultrathin nanofilms with a large specific capacitance and excellent cycling stability open up opportunities for exploring these new 2D materials for flexible energy devices with higher energy density.

RESULTS AND DISCUSSION

Generally, there are some obstacles that block the large-scale preparation of 2D nanostructures: (1) close-packed hexagonal structure or spinel structure will be less inclined to grow along the 2D direction under the influence of unordered intermolecular attraction; (2) avoiding molecular layer agglomeration and precisely limiting the vertical growth of films to the nanoscale have not been conquered yet; (3) addition of organic compounds or the electrodeposition method inevitably affected the purity of the product and complicated the morphology control.[30−33]

In our studies, cobalt–ammonia complexes ($Co[NH_3]_6^{n+}$, n = 2 or 3) will undergo a reconstruction process under hydrothermal conditions, which can be used to fabricate 2D Co_3O_4 nanofilms. The formation mechanism of Co_3O_4 nanofilms is shown in Figure 1. First, based on the coordination theory,[34] the cobalt ion tends to incorporate six ligands (H_2O or NH_3) to form metal complexes with an octahedral structure. As shown in Figure 1, step a, $Co[NH_3]_6^{2+}$ was generated quickly during the room temperature preparation. The transmission electron microscopy (TEM) images and X-ray diffraction (XRD) patterns of samples synthesized at room temperature are shown in Supporting Information Figure S1. In Figure S1a, the spindles exhibited uniform structures and good dispersion. A single spindle of cobalt–ammonia complexes is also presented in Figure S1b. The XRD pattern in Figure S1c revealed that the products were mainly $Co(NO_3)_2$ (JCPDS card no. 19-0356) and $Co(NO_3)_2 \cdot 8H_2O$ (JCPDS card no. 21-0266) because $Co[NH_3]_6(NO_3)_2$ was so unstable even at room temperature that it would lose six NH_3 ligands and become $Co(NO_3)_2$ again during the drying procedure.

Second, the chelating stability coefficients of $Co[NH_3]_6^{2+}$ and $Co[NH_3]_6^{3+}$ are 1.3×10^5 and 3.2×10^{32}, respectively.[34] In the process of hydrothermal reaction, when the temperature began to increase, part of $Co[NH_3]_6^{2+}$ would decompose, and the others would be oxidized to more stable $Co[NH_3]_6^{3+}$ spontaneously due to decomposition of H_2O_2 (as shown in Figure 1, step b). In addition, $Co[NH_3]_6^{3+}$ would reconstruct slowly in boiling water, releasing the unidentate NH_3 ligand.[35] Furthermore, while the $Co[NH_3]_6^{n+}$ (n = 2 or 3) appears as the dominant species in alkaline solution, it greatly benefits the 2D instantaneous nucleation.[36] This process is strongly influenced by the pH of the solution. On this basis, taking into account the comparatively high concentration of NH_3 in this reaction environment, this

would also tremendously accelerate the formation of the membrane structure.[37]

As illustrated in Figure 1, step c, $Co[NH_3]_6^{n+}$ reconstructed into innumerable nanolamellas which served as precursors of nanofilms. Figure S2a depicts, with the samples obtained at the first stage of the hydrothermal process (after hydrothermal treatment for 1 h), that a small number of nanoslices have already emerged in the interlayers of the spindles. A high-magnification TEM image of a nanoslice is shown in the inset of Figure S2a. To our surprise, many nanoslices and a piece of nanofilm also existed in the same samples obtained after hydrothermal treatment for 1 h (Figure S2b). It indicates that the recrystallization of nanofilms already started at this point in time and would last through the whole hydrothermal process. As shown in the XRD pattern in Figure S2c, the samples mainly consisted of $Co[NH_3]_6(NO_3)_3$ (JCPDS card no. 31-0416) and a small number of $Co(NO_3)_2$ (JCPDS card no. 19-0356). It can be inferred that the samples obtained after 1 h were composed of $Co[NH_3]_6(NO_3)_3$ and $Co[NH_3]_6(NO_3)_2$. Meanwhile, the $Co[NH_3]_6(NO_3)_3$ maintained its stability in the samples, while the $Co[NH_3]_6(NO_3)_2$ turned into $Co(NO_3)_2$ in the subsequent drying process.

After newly generated Co_3O_4 underwent a recrystallization process, the Co_3O_4 nanoslices were produced (as illustrated in Figure 1, step d). It is known that the Co_3O_4 unit cell possesses a large *c*-axis distance and charge balance. This characteristic offered us an option on solving the nanoscale control of vertical growth. Researchers have noticed that nitrate is apt to insert into the Co−O bond during hydrothermal conditions.[38] Thus, the nitrate was introduced into our reaction system, which inserted in a timely manner into the Co−O bond as the inhibitor to selectively reduce the growth velocity along the [100] crystal direction. Due to the abundant nitrate and NH_3 that coexist in the hydrothermal solution, the nitrate would affect the growth stage by selectively changing the growth kinetics of the different crystals.[39] The influence mechanism is very similar to the role of surfactants in morphology control of nanostructures.

Finally, under this condition, the as-generated nanoslices continued to merge with each other and stretch along the 2D direction, eventually turning into atomic layer nanofilms (as depicted in Figure 1, step e). This could also be supported by the TEM image of the corresponding reaction process, which is displayed in Figure S2b, accompanying many nanoslices, where a piece of newly generated nanofilm already appeared. Attributed to the molecular isolation role of nitrate, the vertical growth of the nanomembrane was very restricted. Therefore, the ultrathin Co_3O_4 nanofilm could be synthesized. It is worth mentioning that if we remove the step of adding H_2O_2, we would obtain similar ultrathin $Co(OH)_2$ nanofilms rather than Co_3O_4 nanofilms.

Based on the assumptions proposed above, the 2D Co_3O_4 nanofilms were successfully prepared as shown in Figure 2. Owing to the ultralarge size of as-prepared sub-3 nm atomic layer nanofilms, Figure 2a−h show images of every edge of the ultrathin compact Co_3O_4 nanofilms. A wrinkle is observed in Figure 2b, where a similar appearance exists in the graphene structure. It can be seen from all of the TEM images that the curling is very common at the edge of the nanofilm, which results from its ultrathin thickness. As displayed in Figure 2e, an avulsion was spreading quickly due to the release of thermal stress, which was caused by the high-energy electron bombardment. This sub-3 nm atomic layer Co_3O_4 nanofilm exhibited a flat and smooth surface with a large area. The scanning electron microscopy (SEM) image of an ultrathin Co_3O_4 nanofilm is shown in Figure S3. It spread out over a very large area on the substrate (*ca.* 4.00 μm × 10.00 μm). Scanning probe microscopy (SPM) was combined to measure the physical structure parameters of the atomic layer nanofilms. As shown in Figure 2m, based on the viewing zone of 30.00 μm × 30.00 μm, a whole Co_3O_4 nanofilm was detected. Within the scope of the nanofilm with an area of 20.00 μm × 30.00 μm, homogeneous contrast also indicated that the nanofilm has a smooth surface. The analyzer of SPM revealed that uniform thickness of this nanofilm is 2.90 ± 0.10 nm. The identical structure features of the edge curl could be further confirmed by the three-dimensional (3D) surface plot shown in Figure 2f.

High-resolution SPM characterizations were also applied to observe the microscopic surface texture and margin status of sub-3 nm atomic layer Co_3O_4 nanofilms. The nanofilms were finely dispersed on the surface of natural mica (Figure 3a). From the high-resolution 3D SPM image in Figure 3b, the nanoscale surface roughness of natural mica could be observed. On the contrary, this as-prepared sub-3 nm Co_3O_4 nanofilm possesses uniform thickness and high surface smoothness.

To further analyze the crystal structure of sub-3 nm atomic layer nanofilms, the high-resolution transmission electron microscopy (HR-TEM) and selected area electron diffraction (SAED) images were adopted in this study. HR-TEM images are shown in Figure 4a, and the high crystallization feature of the Co_3O_4 nanofilm can be concluded due to its unambiguous lattice fringe image. The distinct fringe spacing of 0.27 nm in Figure 4a corresponds to the (220) crystal plane in the Co_3O_4 spinel structure. The SAED pattern (Figure 4b) indicated that their polycrystalline characteristics and the five concentric diffraction rings from the center could be assigned to (111), (220), (311), (511), and (531) planes of Co_3O_4.

Subsequently, the powder XRD characterization was employed to confirm the constituent of the atomic

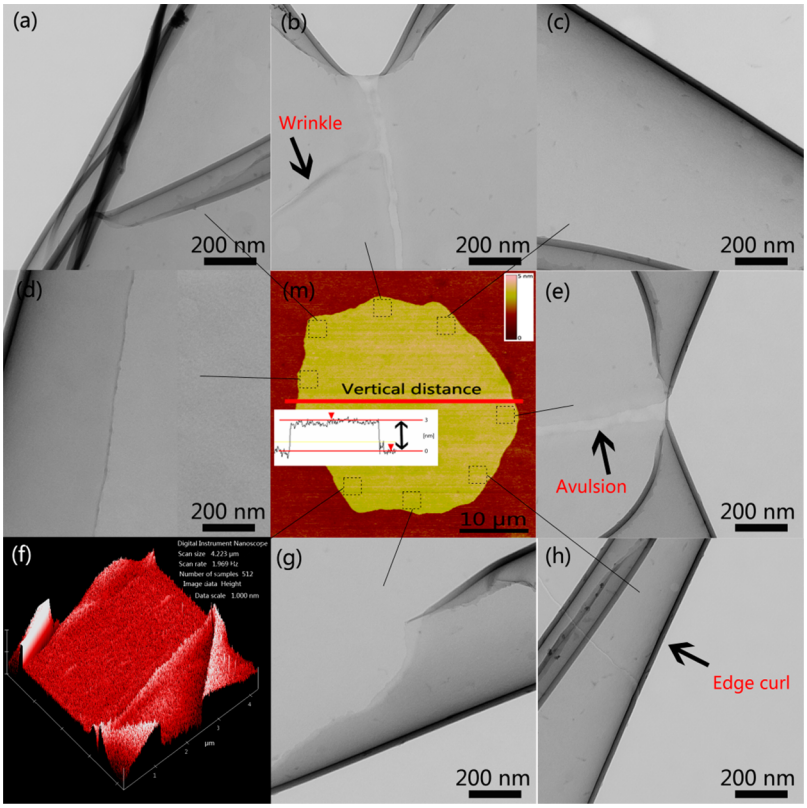

Figure 2. TEM image of (a) top left corner, (b) top, (c) top right, (d) left, (e) right, (g) bottom, and (h) right bottom of our representative Co_3O_4 nanofilms. (f) Three-dimensional surface plot of selected area of nanofilms. (m) SPM image of atomic layer Co_3O_4 nanofilms. The inset is the thickness measurement data.

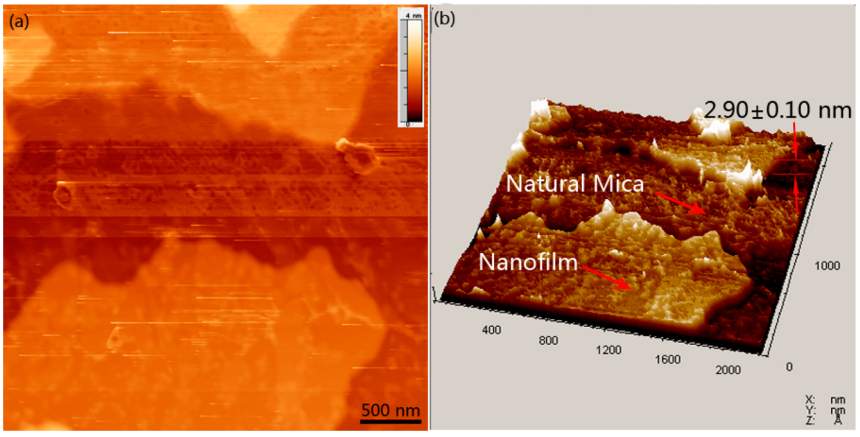

Figure 3. (a) High-resolution top view SPM image of atomic layer Co_3O_4 nanofilms. (b) High-resolution 3D SPM image of atomic layer Co_3O_4 nanofilms.

layer Co_3O_4 nanofilms (as shown in Figure 5a). All of the diffraction peaks could be indexed to the standard PDF card (JCPDS card no. 43-1003), which corresponds with the traits of the cubic spinel Co_3O_4.

The complete survey spectra of Co_3O_4 nanofilms are shown in Figure S4. The main peaks could be indexed to Co 2p, O 1s, and C 1s regions, which implied that no other metallic or inorganic containments were involved in the outcomes. Figure 5b presents high-resolution X-ray photoelectron spectroscopy (XPS) spectra of Co 2p in sub-3 nm Co_3O_4 nanofilms. The Co 2p spectrum exhibits spin−orbit splitting into $2p_{1/2}$ and $2p_{3/2}$ components, and both contained the same chemical information.[40] Hence only the higher intensity Co $2p_{3/2}$ band was curve-fitted. As illustrated in Figure 5b, the peak at 779.4 eV is the exclusive spectrum of Co_3O_4 (according to the XPS binding energy manual). Moreover, the peak at 781.3 eV is strong evidence for Co(II) in Co_3O_4 differentiating from Co(II) in $Co(OH)_2$.[41] More importantly, the band gap of 14.6 eV between $2p_{1/2}$ and $2p_{3/2}$ is a distinctive sign of the XPS spectra of Co_3O_4.

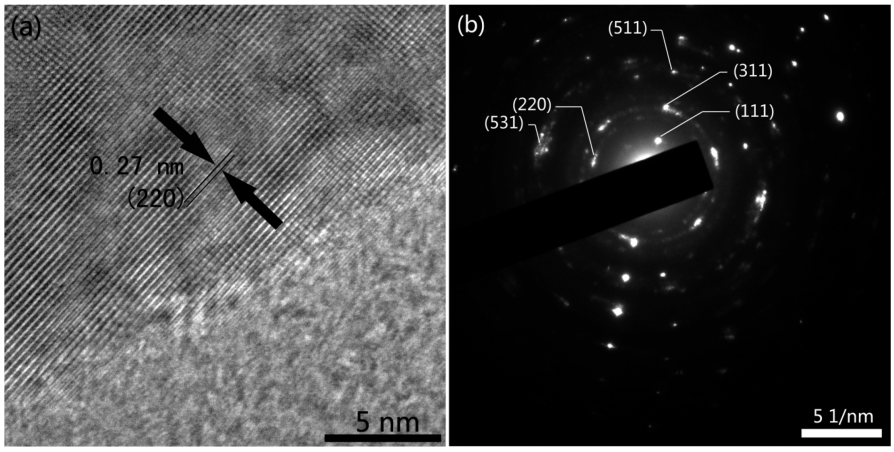

Figure 4. (a) HR-TEM image of atomic layer Co_3O_4 nanofilms. (b) SAED of the corresponding part of the HR-TEM image.

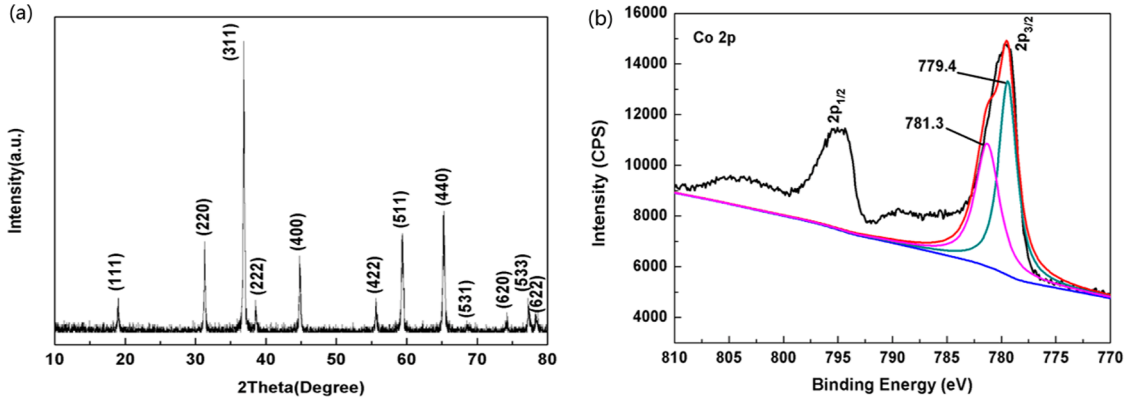

Figure 5. (a) PXRD pattern for atomic layer Co_3O_4 nanofilms. (b) High-resolution XPS spectra of Co 2p in atomic layer Co_3O_4 nanofilms.

To verify the formation mechanism mentioned above, control experiments were designed. According to our research results, the synergistic effect of NH_3 and NO_3^- held the key position of promoting 2D nucleation and growth. Figure S5a shows the products that were prepared by halving the dosage of ammonium hydroxide (10 mL). Obviously, the decrease of dissociative NH_3 directly weakened the driving force of film formation. As a result, only a few slices coexisted with a number of dendritic structures compared to the typical synthesis procedure (20 mL). Figure S5b,c shows the samples obtained by keeping the other parameters constant and replacing the nitrate radicals with the same amount of sulfate and chloride, respectively. As displayed in Figure S5b, a number of regular polyhedrons existed in the final products rather than nanofilms, which indicated that the sulfate radicals surely exerted influences on the selectivity of the crystal plane growth. It was attributed to the size of sulfate being larger than nitrate, resulting in the inability of sulfate to insert into the Co−O bond. When it came to the chloride, the products exhibited sphere-like morphology (Figure S5c). It implied that chloride was unable to affect morphology control. Therefore, it can be concluded that the synthesis of sub-3 nm atomic layer Co_3O_4 nanofilms strongly depended on the mutual influence of free ammonia and nitrate.

In our studies, dosage of nitrate appears to be another determining factor in the nanofilms' morphology control. Influences of different concentrations of nitrate on formation of the products are also discussed. Figure S6a,b represents the products synthesized with a nitrate concentration of 0.5 and 0.75 M, respectively. As shown in Figure S6a, the products were nanosheets with large size, while Figure S6b shows a bunch of sphere-like results. On one hand, a small amount of nitrate would lead to an inadequate capacity to intervene in the vertical stacks; therefore, sheet structure came out as the result of normal stacking. On the other hand, too much nitrate instead totally destroyed the function of dissociative NH_3. Then adjacent nanocrystals aggregated *in situ* and grew into sphere-like structures. Therefore, the appropriate amount (0.625 M) of nitrate is also crucial for preparation of sub-3 nm atomic layer nanofilms.

Hydrothermal temperature and hydrothermal time were also believed to have essential impacts on morphology of the products. In a typical process, 140 °C is the proper temperature to prepare perfect nanofilms. While the temperature was 100 °C, only microspheres

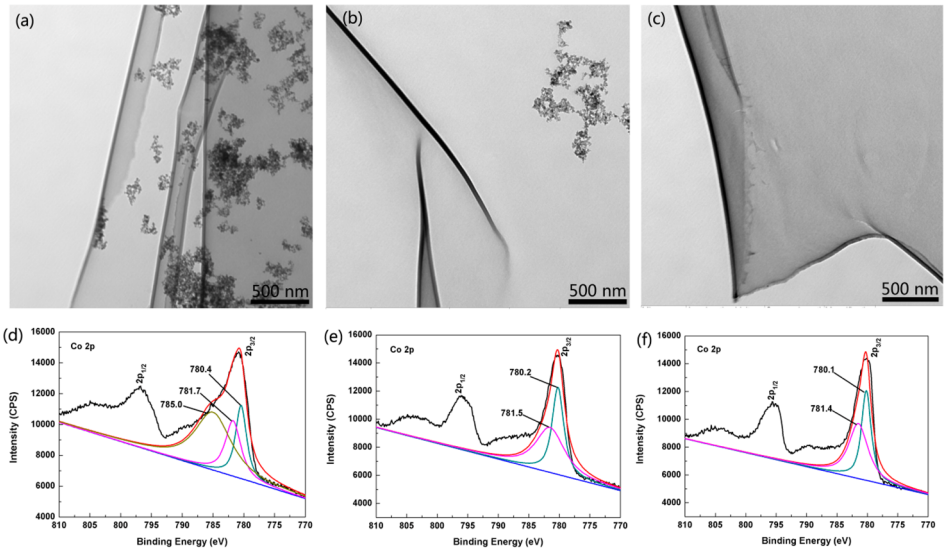

Figure 6. TEM images of the products with a hydrothermal time of (a) 3 h, (b) 6 h, and (c) 9 h. High-resolution XPS spectra of Co 2p in products with a hydrothermal time of (d) 3 h, (e) 6 h, and (f) 9 h.

could be obtained (as shown in Figure S7a). Owing to the low temperature, most of the $Co[NH_3]_6(NO_3)_n$ (n = 2 or 3) did not reconstruct during the hydrothermal process, rendering them ineffective for 2D nucleation promotion. Hence, the synthesis of Co_3O_4 nanospheres held a dominant position again. When the temperature was increased to 120 °C, Co_3O_4 nanofilms were prepared and the accompanying residues of the intermediate remained in the interlayers of nanofilms (as shown in Figure S7b). However, in the course of 12 h, those intermediate nanosheets lacked enough time to incorporate with each other and build a nanofilm. The TEM image of products synthesized at the hydrothermal temperature of 160 °C is displayed in Figure S7c, which indicates that only debris-like nanoplatelets could be obtained at this condition. It could possibly be ascribed to ammonia ionization under high temperature. There was not enough dissociative NH_3 to prompt the nanofilm formation. As a result, most of the nanoplatelets agglomerated and remained in the final products when the reaction was terminated.

In the mechanism analysis proposed earlier, both of the TEM images and XRD patterns proved that the products obtained at room temperature and in the first stage (after a hydrothermal process for 1 h) were $Co[NH_3]_6(NO_3)_2$ and $Co[NH_3]_6(NO_3)_n$ (n = 2 or 3), respectively. In order to further uncover the whole process of nanofilm formation, products of various hydrothermal times were investigated. The XRD patterns of the products obtained in a hydrothermal process of 3, 6, and 9 h are shown in Figure S8. Although the products showed poor crystalline characteristics, all of them could be indexed to spinel Co_3O_4 (JCPDS card no. 43-1003). The TEM images of products obtained at 3, 6, and 9 h are displayed in Figure 6a−c, respectively. With the increase of time, the gradual decrease of intermediate products indicated the ongoing nanofilm formation. Meanwhile, XPS analysis was adopted to probe the composition change of the samples during the hydrothermal process. The comparatively higher binding energy peak at 785.0 eV in Figure 6d (3 h) could be attributed to Co(II) in the cobalt−ammonia complexes that had not dissociated yet, and the corresponding peak disappeared in Figure 6e (6 h) because most of the cobalt−ammonia complexes had already transformed into Co_3O_4 under the hydrothermal conditions. The further right shift of peaks in Figure 6f (9 h) illustrate the continuous signal enhancement of Co(III) in Co_3O_4. The transformation process of $Co(NO_3)_2 \rightarrow Co[NH_3]_6(NO_3)_2 \rightarrow Co[NH_3]_6(NO_3)_n$ (n = 2 or 3) $\rightarrow Co_3O_4$ was fully demonstrated and proved.

In the transition of $Co[NH_3]_6^{2+}$ to $Co[NH_3]_6^{3+}$, the H_2O_2 played an important role at an incipient stage of the hydrothermal reaction. When we kept other parameters constant and removed H_2O_2, the reaction product would be $Co(OH)_2$ atomic layer nanofilms rather than Co_3O_4 atomic layer nanofilms. The TEM images of $Co(OH)_2$ nanofilms are shown in Figure 7a,b. As depicted in Figure 7a, the atomic layer nanofilms possess an intact structure, and most of the nanofilms closely adhere to the substrate due to their ultrathin feature. The inset of Figure 7a is the amplified TEM image of the wrinkle. As shown in the higher-magnification TEM image in Figure 7b, these atomic layer $Co(OH)_2$ nanofilms exhibit a flat and smooth surface with a large area and the apparent curls were visible. The uniformity of contrast indicates that the thickness of the nanofilm is very homogeneous.

As displayed in Figure 7c, the unambiguous lattice fringe image indicates that the atomic layer $Co(OH)_2$ nanofilm is composed of many nanocrystallines. The distinct fringe spacing of 0.23 nm in Figure 7c

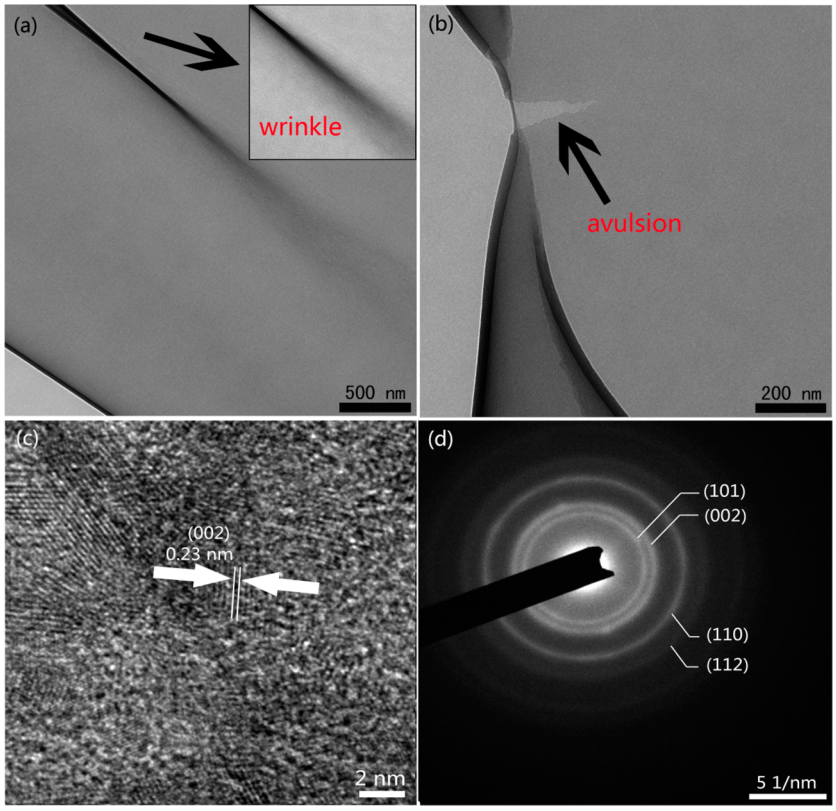

Figure 7. (a) Low-magnification TEM image of atomic layer $Co(OH)_2$ nanofilms; the inset is the amplified part of the TEM image of the wrinkle. (b) High-magnification TEM image of atomic layer $Co(OH)_2$ nanofilms. (c) HR-TEM image of atomic layer $Co(OH)_2$ nanofilms. (d) SAED of corresponding part of the HR-TEM.

corresponds to the (002) crystal plane of β-$Co(OH)_2$. The SAED pattern (Figure 7d) further confirms their polycrystalline characteristics. The four concentric diffraction rings from the center can be assigned to (101), (002), (110), and (112) planes of β-$Co(OH)_2$. A corresponding XRD pattern and SPM image are shown in Figure S9. All of the diffraction peaks (Figure S9a) are consistent with the brucite-like phase of β-$Co(OH)_2$, according to the standard PDF cards (JCPDS card no. 30-0443). As shown in Figure S9b, based on the viewing zone of 30.00 μm $\times$ 30.00 μm, a whole $Co(OH)_2$ nanofilm was detected. Within the scope of the nanofilm with an area of 25.00 μm $\times$ 5.00 μm, homogeneous contrast also indicates that the nanofilm has a smooth surface and the uniform thickness is 3.70 $\pm$ 0.10 nm.

The electrochemical performances of sub-3 nm atomic layer Co_3O_4 nanofilms were evaluated as a cathode material for supercapacitor application successively. The powders that were loaded on the nickel foam serve as the positive electrode. As seen in Figure 8a, the scan range was set between -0.4 and 0.8 V (*vs* saturated calomel electrode) and scan rate was set at 5, 10, 20, 50, and 100 mV/s. Accompanying the increase of the scan rate, the peak currents also increased, which suggested the good reversibility of the fast charge$-$discharge response of the materials. It is observed from the cyclic voltammogram (CV) curves that the pseudocapacitance of the atomic layer Co_3O_4 is completely different from the trait of traditional electric double-layer capacitors which reflects the lack of a symmetry of curves.

The first galvanostatic charge$-$discharge test was run in the potential range of 0 to 0.47 V with a charging and discharging current set at different densities (as shown in Figure 8b). The specific capacitance of the supercapacitors could be calculated from the charge/discharge test together with the following equation.[42]

$$C_m = I \cdot \Delta t / m \cdot \Delta V \quad (1)$$

where C_m is the specific capacitance of the capacitor (F/g); I is the current of the charge/discharge; Δt is the discharging time period in seconds for the potential change ΔV, in volts; m is the mass load of the active material. All of the electrochemical measurements were carried out at room temperature.

From Figure 8b,c, according to eq 1 mentioned above, the specific capacitance of atomic layer Co_3O_4 nanofilms could be calculated to 1400, 1376, 1340, and 1276 F/g at a current density of 1, 2, 4, and 8 A/g, respectively. The slight decrease of capacitance with the increase of the charge/discharge current indicates that the materials allowed the redox reaction to take place rapidly at high galvanostatic current densities. As indicated by the error bar in Figure 8c, the four values are average data that correspond to different current

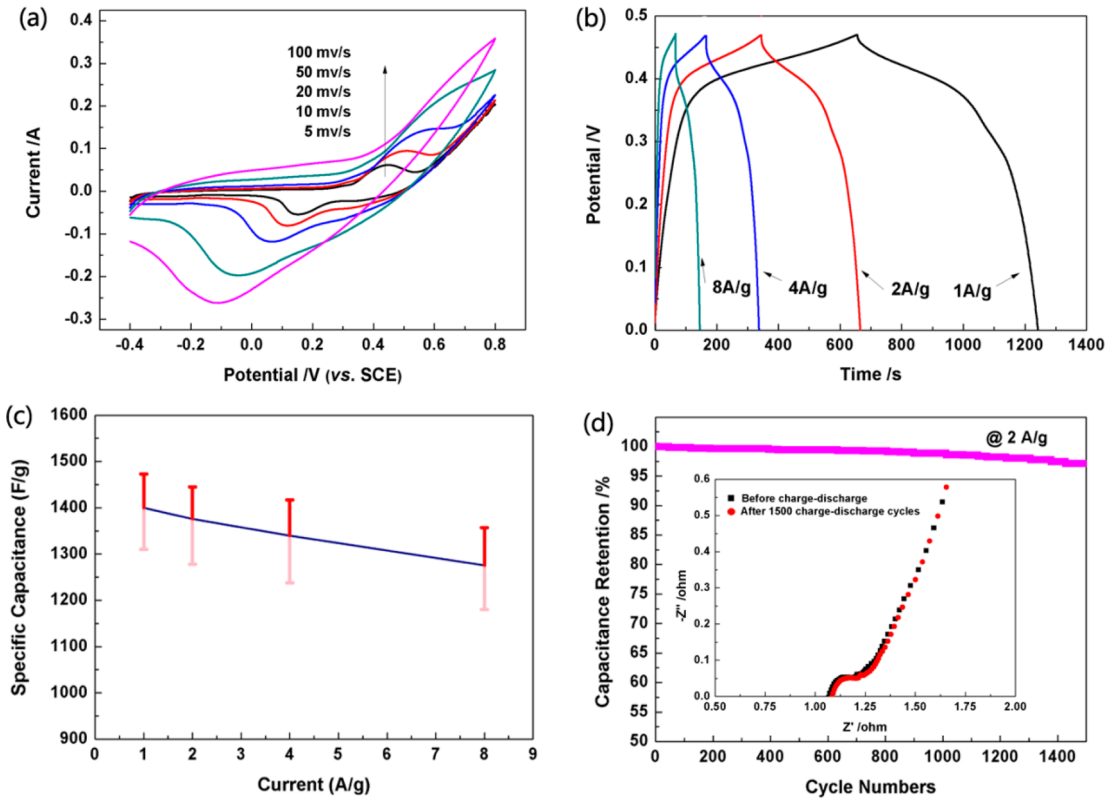

Figure 8. (a) Cyclic voltammograms of the atomic layer Co_3O_4 nanofilms in KOH electrolyte at various scan rates of 5, 10, 20, 50, and 100 mV/s. (b) Charge−discharge curves of the atomic layer Co_3O_4 nanofilms measured at different current densities. (c) Average specific capacitance of the atomic layer Co_3O_4 nanofilms at various discharge current densities with error bar. (d) Cycle test of atomic layer Co_3O_4 nanofilms with a galvanostatic charge−discharge current density of 2 A/g; the inset is the electrochemical impedance spectra before and after 1500 cycling tests.

densities. The details of the experimental data are given in Table S1. Figure 8d shows the 1500 cycling test data of sub-3 nm atomic layer Co_3O_4 nanofilms at a galvanostatic charge−discharge current density of 2 A/g within the potential window of 0−0.47 V. Only a small decrease of the capacitance (2.9%) could be observed, which resulted from the consumption of electrolyte caused by the irreversible reaction between the electrode materials and electrolyte (as shown in the inset of Figure 8d). Corresponding supercapacitor performance characterization of atomic layer $Co(OH)_2$ nanofilms was also carried out, and the details of these results are shown in Figure S10. The specific capacitance of ultrathin $Co(OH)_2$ nanofilms was calculated to be 1076, 1000, 974, and 870 F/g at a current density of 1, 2, 4, and 8 A/g, respectively. In the end, the charge and discharge cycling test was also performed with a galvanostatic charge and discharge current density of 2 A/g. The results show that specific capacitance of atomic layer $Co(OH)_2$ nanofilms slightly decreased 1.9% after the cycling test was repeated 1500 times, as displayed in Figure S10d.

In short, the high specific capacitance of as-prepared electrode materials could be attributed to the unique nanostructures of sub-3 nm atomic layer Co_3O_4 nanofilms. The ultrathin thickness of nanofilms not only greatly benefits the ion transport but also provides far more electrochemical active sites than traditional nanostructures. Consequently, the efficiency of electrochemical reactions increases dramatically. Due to the nanoscale thickness of nanofilms, thermal expansion that results from the charge/discharge process can be negligible. Therefore, the electrode structure basically remains intact after a long cycling test. This explains why the capacitance hardly degraded even after 1500 charge/discharge processes. As for the performance advantage of Co_3O_4 nanofilms (1400 F/g) over $Co(OH)_2$ nanofilms (1076 F/g), the improvement should be attributed to the addition of Co(III). It is believed that the Co(III) could better explore the potential of cobalt oxide materials in supercapacitor applications by improving the efficiency of energy conversion during the redox reaction.

CONCLUSIONS

In this paper, we applied a novel approach that takes advantage of a hydrothermal reaction assisted by cobalt−ammonia complexes and nitrate to prepare Co_3O_4 nanofilms. We successfully prepared large-sized and smooth Co_3O_4 nanofilms with sub-3 nm atomic layer thickness without any substrate or surfactant. The as-obtained Co_3O_4 nanofilms showed high specific capacitance (1400 F/g) and excellent cycling stability in performance tests. In view of the

large size and ultrathin thickness, the atomic layer Co_3O_4 nanofilms are surely believed to have huge potentials in the application of supercapacitors and wearable devices.

METHODS

Chemicals. Cobalt nitrate ($Co(NO_3)_2$, analytical grade), cobalt sulfate ($CoSO_4$, analytical grade), cobalt chloride ($CoCl_2$, analytical grade), sodium nitrate ($NaNO_3$, ≥99.5%), sodium sulfate (Na_2SO_4, ≥99.5%), sodium chloride (NaCl, ≥99.5%), ammonium hydroxide ($NH_3 \cdot H_2O$, 25−28%), and hydrogen peroxide (H_2O_2) were used. All reagents were purchased from Sinopharm Chemical Reagent Co., Ltd. and were used as received. The deionized water used in all experiments with a resistivity of 18.2 MΩ·cm was prepared using an ultrapure water system (Millipore).

Preparation of Sub-3 nm Atomic Layer Co_3O_4 Nanofilms. In a typical synthesis, 10 mM $Co(NO_3)_2$ and 5 mM $NaNO_3$ were dissolved in 20.0 mL of deionized water to form homogeneous solution. Then 20 mL of $NH_3 \cdot H_2O$ was added dropwise to the mixed solution with constant stirring in air for about 10 min. Subsequently, after the addition of 2 mL of H_2O_2 and constant stirring for another 10 min, the mixture was sealed in a 200 mL Teflon-lined stainless steel autoclave and transferred into a homogeneous reactor set at 140 °C for 12 h. By the time the reactor cooled to room temperature, the samples were rinsed three times with deionized water and ethanol and dried in a conventional oven. Then the black powders were obtained.

Material Characterization. Transmission electron microscopic investigation was carried out using a high-resolution transmission electron microscope (JEOL, JEM-2100F) operated at 200 kV. All samples were dispersed in absolute ethanol solution and then dropped on a copper grid. SAED was also performed on the previous TEM. The phase purity of the as-prepared sample was characterized by X-ray diffraction (D/max 2550VL/PC) with Cu Kα radiation from 10 to 80° at a scanning rate of 4°/min. The X-ray tube voltage and current were set at 35 kV and 200 mA, respectively. The surface topography and thickness of nanofilms were viewed on an environment control scanning probe microscope (SII Nanonavi E-Sweep), in which the longitudinal and lateral resolution is 0.03 and 1 nm, respectively. XPS data were acquired using a Kratos AXIS Ultra X-ray photoelectron spectroscope incorporating a 165 mm hemispherical electron energy analyzer. The incident radiation was monochromatic Al Kα X-rays at 150 W. Survey (wide) scans were taken at an analyzer pass energy of 160 eV and multiplex (narrow) high-resolution scans of Co 2p, O 1s, and C 1s at a pass energy of 40 eV. Survey scans were carried out over 1200−0 eV binding energy range with 1.0 eV steps and a dwell time of 100 ms. Narrow high- resolution scans were run with 0.1 eV steps and 162 ms dwell time.

Electrochemical Measurements. The electrochemical studies were performed in a conventional three-electrode system with a KOH electrolyte solution (2 mol/L). The newly produced atomic layer Co_3O_4 nanofilms loaded on nickel foams, a platinum electrode, and a saturated calomel electrode were used as the working electrode, counter electrode, and reference electrode, respectively. The working electrode was composed of active Co_3O_4 materials (75 wt %), carbon black (15 wt %), and binder (PTFE, 10 wt %). The mixture was first coated onto the surface of a piece of nickel foam sheet (1 cm × 1 cm) and dried at 80 °C overnight. The sheets with active materials were finally pressed under 14 MPa to obtain the working electrode. The CV and galvanostatic charge/discharge cycle tests were performed on a CHI 660E electrochemical workstation.

Conflict of Interest: The authors declare no competing financial interest.

Supporting Information Available: TEM images and XRD patterns of cobalt−ammonia complexes; TEM images and XRD patterns of cobalt−ammonia complexes and transient state; SEM images of Co_3O_4 nanofilms; complete survey spectra of atomic layer Co_3O_4 nanofilms; TEM image of the products of the control group which halved the dosage of ammonium hydroxide (10 mL), replaced all the nitrate radicals with same amount of sulfate, and replaced all the nitrate radicals with the same amount of chloride; TEM images of products of the control group for which nitrate was insufficient (0.5 M) and superfluous (0.75 M) during the synthesis process; TEM images of the products for which the hydrothermal temperatures were 100, 120, and 160 °C; XRD patterns of products obtained at hydrothermal times of 3, 6, and 9 h; PXRD pattern and SPM image of atomic layer $Co(OH)_2$ nanofilms; table showing details of experimental data of the first charge−discharge test of atomic layer Co_3O_4 nanofilm samples at various current densities; electrochemical characterization of atomic layer $Co(OH)_2$ nanofilms. This material is available free of charge *via* the Internet at http://pubs.acs.org.

Acknowledgment. This work was supported by the National Science Fund for Distinguished Young Scholars (No. 51125016), and the National Natural Science Foundation of China (Nos. 51472178 and 51371119).

REFERENCES AND NOTES

1. Zhang, L.; Wu, H. B.; Madhavi, S.; Hng, H. H.; Lou, X. W. Formation of Fe_2O_3 Microboxes with Hierarchical Shell Structures from Metal-Organic Frameworks and Their Lithium Storage Properties. *J. Am. Chem. Soc.* **2012**, *134*, 17388–17391.
2. Goodenough, J. B.; Park, K. S. The Li-Ion Rechargeable Battery: A Perspective. *J. Am. Chem. Soc.* **2013**, *135*, 1167–1176.
3. Kim, K. S.; Zhao, Y.; Jang, H.; Lee, S. Y.; Kim, J. M.; Kim, K. S.; Ahn, J. H.; Kim, P.; Choi, J. Y.; Hong, B. H. Large-Scale Pattern Growth of Graphene Films for Stretchable Transparent Electrodes. *Nature* **2009**, *457*, 706–710.
4. Kim, Y. H.; Heo, J. S.; Kim, T. H.; Park, S.; Yoon, M. H.; Kim, J.; Oh, M. S.; Yi, G. R.; Noh, Y. Y.; Park, S. K. Flexible Metal-Oxide Devices Made by Room-Temperature Photochemical Activation of Sol−Gel Films. *Nature* **2012**, *489*, 128-U191.
5. Crossland, E. J. W.; Noel, N.; Sivaram, V.; Leijtens, T.; Alexander-Webber, J. A.; Snaith, H. J. Mesoporous TiO_2 Single Crystals Delivering Enhanced Mobility and Optoelectronic Device Performance. *Nature* **2013**, *495*, 215–219.
6. Ahn, B. Y.; Duoss, E. B.; Motala, M. J.; Guo, X. Y.; Park, S. I.; Xiong, Y. J.; Yoon, J.; Nuzzo, R. G.; Rogers, J. A.; Lewis, J. A. Omnidirectional Printing of Flexible, Stretchable, and Spanning Silver Microelectrodes. *Science* **2009**, *323*, 1590–1593.
7. Tian, B. Z.; Cohen-Karni, T.; Qing, Q.; Duan, X. J.; Xie, P.; Lieber, C. M. Three-Dimensional, Flexible Nanoscale Field-Effect Transistors as Localized Bioprobes. *Science* **2010**, *329*, 830–834.
8. El-Kady, M. F.; Strong, V.; Dubin, S.; Kaner, R. B. Laser Scribing of High-Performance and Flexible Graphene-Based Electrochemical Capacitors. *Science* **2012**, *335*, 1326–1330.
9. Britnell, L.; Ribeiro, R. M.; Eckmann, A.; Jalil, R.; Belle, B. D.; Mishchenko, A.; Kim, Y. J.; Gorbachev, R. V.; Georgiou, T.; Morozov, S. V.; et al. Strong Light−Matter Interactions in Heterostructures of Atomically Thin Films. *Science* **2013**, *340*, 1311–1314.
10. Zhang, X.; Ma, W.; Nan, H.; Wang, G. Ultrathin Zinc Oxide Nanofilm on Zinc Substrate for High Performance Electrochemical Sensors. *Electrochim. Acta* **2014**, *140*, 186–193.
11. Kao, J.; Thorkelsson, K.; Bai, P.; Zhang, Z.; Sun, C.; Xu, T. Rapid Fabrication of Hierarchically Structured Supramolecular Nanocomposite Thin Films in One Minute. *Nat. Commun.* **2014**, *5*, 4053.
12. Sumboja, A.; Foo, C. Y.; Wang, X.; Lee, P. S. Large Areal Mass, Flexible and Free-Standing Reduced Graphene

Oxide/Manganese Dioxide Paper for Asymmetric Supercapacitor Device. *Adv. Mater.* **2013**, *25*, 2809–2815.
13. Liu, Y. X.; Dai, H. X.; Deng, J. G.; Xie, S. H.; Yang, H. G.; Tan, W.; Han, W.; Jiang, Y.; Guo, G. S. Mesoporous Co_3O_4-Supported Gold Nanocatalysts: Highly Active for the Oxidation of Carbon Monoxide, Benzene, Toluene, and *o*-Xylene. *J. Catal.* **2014**, *309*, 408–418.
14. Bao, L. H.; Zang, J. F.; Li, X. D. Flexible Zn_2SnO_4/MnO_2 Core/Shell Nanocable-Carbon Microfiber Hybrid Composites for High-Performance Supercapacitor Electrodes. *Nano Lett.* **2011**, *11*, 1215–1220.
15. Li, X. C.; Siegbahn, P. E. M. Water Oxidation Mechanism for Synthetic Co-Oxides with Small Nuclearity. *J. Am. Chem. Soc.* **2013**, *135*, 13804–13813.
16. Chen, Z.; Augustyn, V.; Wen, J.; Zhang, Y. W.; Shen, M. Q.; Dunn, B.; Lu, Y. F. High-Performance Supercapacitors Based on Intertwined CNT/V_2O_5 Nanowire Nanocomposites. *Adv. Mater.* **2011**, *23*, 791–795.
17. Liu, X. H.; Ma, R. Z.; Bando, Y.; Sasaki, T. A General Strategy to Layered Transition-Metal Hydroxide Nanocones: Tuning the Composition for High Electrochemical Performance. *Adv. Mater.* **2012**, *24*, 2148–2153.
18. Koza, J. A.; Hull, C. M.; Liu, Y. C.; Switzer, J. A. Deposition of β-$Co(OH)_2$ Films by Electrochemical Reduction of Tris-(ethylenediamine)cobalt(III) in Alkaline Solution. *Chem. Mater.* **2013**, *25*, 1922–1926.
19. Wang, L.; Dong, Z. H.; Wang, Z. G.; Zhang, F. X.; Jin, J. Layered -$Co(OH)_2$ Nanocones as Electrode Materials for Pseudocapacitors: Understanding the Effect of Interlayer Space on Electrochemical Activity. *Adv. Funct. Mater.* **2013**, *23*, 2758–2764.
20. Xu, L. P.; Ding, Y. S.; Chen, C. H.; Zhao, L. L.; Rimkus, C.; Joesten, R.; Suib, S. L. 3D Flowerlike α-Nickel Hydroxide with Enhanced Electrochemical Activity Synthesized by Microwave-Assisted Hydrothermal Method. *Chem. Mater.* **2008**, *20*, 308–316.
21. Li, J. X.; Yang, M.; Wei, J. P.; Zhou, Z. Preparation and Electrochemical Performances of Doughnut-like $Ni(OH)_2$-$Co(OH)_2$ Composites as Pseudocapacitor Materials. *Nanoscale* **2012**, *4*, 4498–4503.
22. Chang, J. K.; Wu, C. M.; Sun, I. W. Nano-architectured $Co(OH)_2$ Electrodes Constructed Using an Easily-Manipulated Electrochemical Protocol for High-Performance Energy Storage Applications. *J. Mater. Chem.* **2010**, *20*, 3729–3735.
23. Feng, J.; Zeng, H. C. Size-Controlled Growth of Co_3O_4 Nanocubes. *Chem. Mater.* **2003**, *15*, 2829–2835.
24. Kung, C. W.; Chen, H. W.; Lin, C. Y.; Vittal, R.; Ho, K. C. Synthesis of Co_3O_4 Nanosheets *via* Electrodeposition Followed by Ozone Treatment and Their Application to High-Performance Supercapacitors. *J. Power Sources* **2012**, *214*, 91–99.
25. Zhang, B.; Zhang, Y. B.; Miao, Z. Z.; Wu, T. X.; Zhang, Z. D.; Yang, X. G. Micro/Nano-structure Co_3O_4 as High Capacity Anode Materials for Lithium-Ion Batteries and the Effect of the Void Volume on Electrochemical Performance. *J. Power Sources* **2014**, *248*, 289–295.
26. Fan, Y. Q.; Fan, L. F.; Meng, S. M.; Guo, Y.; Liu, Y. W. Preparation of Cobalt Hydroxide Film Modified Electrode and Its Analytical Application. *J. Anal. Chem.* **2012**, *67*, 370–377.
27. Cook, J. G.; van der Meer, M. P. The Optical Properties of Sputtered Co_3O_4 Films. *Thin Solid Films* **1986**, *144*, 165–176.
28. Srinivasan, V.; Weidner, J. W. Capacitance Studies of Cobalt Oxide Films Formed *via* Electrochemical Precipitation. *J. Power Sources* **2002**, *108*, 15–20.
29. Duan, B. R.; Cao, Q. Hierarchically Porous Co_3O_4 Film Prepared by Hydrothermal Synthesis Method Based on Colloidal Crystal Template for Supercapacitor Application. *Electrochim. Acta* **2012**, *64*, 154–161.
30. Makiura, R.; Motoyama, S.; Umemura, Y.; Yamanaka, H.; Sakata, O.; Kitagawa, H. Surface Nano-architecture of a Metal-Organic Framework. *Nat. Mater.* **2010**, *9*, 565–571.
31. Lin, S. C.; Lee, Y. L.; Chang, C. H.; Shen, Y. J.; Yang, Y. M. Quantum-Dot-Sensitized Solar Cells: Assembly of CdS-Quantum-Dots Coupling Techniques of Self-Assembled Monolayer and Chemical Bath Deposition. *Appl. Phys. Lett.* **2007**, *90*, 143517.
32. Malvadkar, N. A.; Hancock, M. J.; Sekeroglu, K.; Dressick, W. J.; Demirel, M. C. An Engineered Anisotropic Nanofilm with Unidirectional Wetting Properties. *Nat. Mater.* **2010**, *9*, 1023–1028.
33. Huang, H. J.; Pierstorff, E.; Osawa, E.; Ho, D. Protein-Mediated Assembly of Nanodiamond Hydrogels into a Biocompatible and Biofunctional Multilayer Nanofilm. *ACS Nano* **2008**, *2*, 203–212.
34. Sun, W. Y. *Coordination Chemistry*; Chemical Industry Press: Beijing, China, 2010; pp 22−23.
35. Morgan, K.; Gainsford, G.; Milestone, N. A New Type of Layered Aluminium Phosphate $[NH_4]_3[Co(NH_3)_6]_3[Al_2(PO_4)_4]_2$ Assembled about a Cobalt (III) Hexammine Complex. *Chem. Commun.* **1997**, *1*, 61–62.
36. Grujicic, D.; Pesic, B. Electrochemical and AFM Study of Cobalt Nucleation Mechanisms on Glassy Carbon from Ammonium Sulfate Solutions. *Electrochim. Acta* **2004**, *49*, 4719–4732.
37. Hoshino, K.; Hitsuoka, Y. One-Step Template-Free Electrosynthesis of Cobalt Nanowires from Aqueous $Co(NH_3)_6Cl_3$ Solution. *Electrochem. Commun.* **2005**, *7*, 821–828.
38. Zhang, H.; Wu, J. B.; Zhai, C. X.; Ma, X. Y.; Du, N.; Tu, J. P.; Yang, D. R. From Cobalt Nitrate Carbonate Hydroxide Hydrate Nanowires to Porous Co_3O_4 Nanorods for High Performance Lithium-Ion Battery Electrodes. *Nanotechnology* **2008**, *19*, 035711.
39. Qian, L. W.; Zai, J. T.; Chen, Z.; Zhu, J.; Yuan, Y. P.; Qian, X. F. Control of the Morphology and Composition of Yttrium Fluoride *via* a Salt-Assisted Hydrothermal Method. *CrystEngComm* **2010**, *12*, 199–206.
40. Artyushkova, K.; Levendosky, S.; Atanassov, P.; Fulghum XPS Structural Studies of Nano-composite Non-platinum Electrocatalysts for Polymer Electrolyte Fuel Cells. *J. Top. Catal.* **2007**, *46*, 263–275.
41. Yang, J.; Liu, H. W.; Martens, W. N.; Frost, R. L. Synthesis and Characterization of Cobalt Hydroxide, Cobalt Oxyhydroxide, and Cobalt Oxide Nanodiscs. *J. Phys. Chem. C* **2010**, *114*, 111–119.
42. Kim, Y. K.; Cha, S. I.; Hong, S. H. Nanoporous Cobalt Foam and a Co/$Co(OH)_2$ Core−Shell Structure for Electrochemical Applications. *J. Mater. Chem. A* **2013**, *1*, 9802–9808.